Electrodeposition of bismuth, tellurium and bismuth telluride through sub-10 nm mesoporous silica thin films

Li Shao [a,*], Nikolay Zhelev [a], Wenjian Zhang [a], Gillian Reid [a], Ruomeng Huang [b], Philip N. Bartlett [a], Andrew L. Hector [a,*]

[a] School of Chemistry, University of Southampton, Highfield, Southampton SO17 1BJ, UK
[b] School of Electronics and Computer Science, University of Southampton, Southampton, SO17 1BJ, UK

ARTICLE INFO

ABSTRACT

Templated electrodeposition is an efficient technique for the bottom-up fabrication of nanostructures and can effectively control the size and shape of the electrodeposits. Here, mesoporous silica thin films with highly ordered mesopores and a regular three-dimensional mesostructure were synthesised as templates for electrodeposition. The mesoporous silica films have small mesopores ($\sim$8 nm) and complex mesopore channels (*Fmmm* mesostructure with the [0 1 0] axis perpendicular to the substrate). Electrodeposition of bismuth, tellurium and bismuth-tellurium was investigated from electrolytes containing $[N^nBu_4][BiCl_4]$, $[N^nBu_4]_2[TeCl_6]$ and $[N^nBu_4]Cl$ dissolved in dry dichloromethane. Top-view SEM images showed Bi, Te and Bi doped-Te nanoparticles in the mesopores and cross-section SEM showed there were a few Te nanowires, in addition to the particle aggregations on the surface. This is a promising observation as it demonstrates the possibility of preparing sub-10 nm nanowires by templated electrodeposition even though the deposits are not uniformly electrodeposited in all the mesopores. EDX shows the deposited Bi-Te nanoparticles were tellurium-rich, XRD shows they were trigonal tellurium (ICSD 65692). A variety of parameters including the choice of pulsed electrodeposition conditions and $[N^nBu_4][BiCl_4]$ concentration (2.25 mM and 3 mM) were investigated in order to control the composition of the deposit. All samples prepared by pulsed electrodeposition showed very low Bi:Te ratio (Bi/Te$<$0.02), whereas samples deposited for 5 min at -0.6 V achieved high Bi content (Bi/Te$=$0.49).

1. Introduction

Bismuth has a small band overlap (38 meV), small effective mass ($\sim$0.001 me), long mean free path ($\sim$1 mm) and large Fermi wavelength ($\sim$70 nm). These contribute to unusual transport phenomena in Bi nanomaterials, such as high electrical and magnetoresistance, bipolar electrical resistivity and conductive surface states [1-3]. Tellurium is a well-known p-type semiconductor with a narrow indirect bandgap (0.33 eV), and shows some semimetal properties [4]. The semiconducting features of Te make it widely applied in thermoelectric devices [5], solar cells [6], photoconductors [7], gas sensors [8] and piezoelectric energy harvesters [9]. Several tellurium nanostructures with different shapes and sizes have been reported over recent years. Bismuth telluride (Bi_2Te_3) is one of the most efficient thermoelectric materials [10]. It is also a well-studied topological insulator [11]. The properties of bismuth, tellurium and bismuth telluride nanomaterials are significantly altered by their morphologies and dimensions. As a result, zero to three dimensional bismuth, tellurium and bismuth telluride nanomaterials have been fabricated using a variety of "top-down" and "bottom-up" methods, including hydrothermal and solvothermal methods [12], electron-beam irradiation [13], microwave assisted synthesis [14-15], physical vapour deposition [16-17], chemical reduction [18], and electrodeposition [19-24].

The synthesis approach of using pore channels as the template for electrodeposition is called templated electrodeposition. Published work generally uses commercial track-etched polycarbonate (PC) membranes or porous anodic aluminium oxide membranes (AAO) as templates [25]. Using electrodeposition with AAO templates, Jin et al. successfully fabricated uniform, single-crystal bismuth nanowire arrays with a high filling rate and large area ($\sim$75 mm^2), the average nanowire diameter was 60 nm [26]; Zhao et al. fabricated $\sim$60 nm amorphous Te nanowires [21]; Bartlett et al. produced Te nanowires of diameter ranging from 13 nm to 55 nm and tens of micrometres in length, through supercritical difluoromethane-based electrodeposition into AAO templates [27].

Most of the diameters of the resulting nanowires are above 20 nm due to the limitation of the porous templates. Martin-Gonzalez's group achieved small electrodeposited Bi_2Te_3 nanowires, down to 15 nm, by electrodeposition into modified AAO templates [28]. On the other hand, mesoporous silica films are excellent candidates as templates for electrodeposition as they have tuneable pore sizes and structures, high specific surface areas, and high pore volumes [29].

The morphology and size of nanostructures can significantly influence their properties. For example, for thermoelectric materials Bi and Bi_2Te_3, theory predicts that characteristic length scales of <10 nm are necessary to achieve high thermoelectric figures of merit ($ZT > 3$), which encourages the current work to focus on fabricating nanowires of the smallest diameter possible, along with controlling other parameters such as crystallinity and stoichiometry [30-31]. For high-performance transistors, gate-tunability requests to reduce the dimension of tellurium nanostructures [30,32]. By tuning the surfactants used to prepare the mesoporous silica films, the resulting mesopore size can be adjusted between 2 and 30 nm [33], which is generally smaller than the pores of AAO membranes (20 nm to 400 nm)[34] or PC track-etch membranes (20 nm to 14 μm) [35]. Synthesis of nanostructures with sub 10 nm size is difficult with AAO and track-etch membranes. Moreover, AAO membranes only have cylindrical and vertical pore channels, whereas mesoporous silica films can be made with a variety of mesostructures with 3D interconnected pores, vertical or horizontal pores, or lamellar structures [33]. Hence, mesoporous silica films have significant advantages and potential for the templated electrodeposition of nanomaterials. When using mesoporous silica films as templates, arrays of Au and Pt nanoparticles (2.5 nm diameter) have been produced in one-dimensional mesopores (pore diameter 2.7 nm) [36].

Electrodeposition of bismuth, tellurium and bismuth telluride has been widely investigated from aqueous solution. A non-aqueous electrolyte system of tetrabutylammonium halometallate salts dissolved in the organic solvent dichloromethane (CH_2Cl_2, DCM) was introduced in our previous work in 2013 [23]. DCM has low surface tension and viscosity, making it a promising solvent to electrodeposit materials into nanopatterned substrates or templates. Tetrabutylammonium halometallate salts have high solubility in DCM, allowing preparation of electrolytes with high concentration. The precursor species of the electrolyte are all chlorometallate salts and thus they are compatible with each other, allowing alloys to be made by combining the relevant chlorometallates in appropriate ratios. Based on this system, a variety of p-block materials including In, Sb, Se, Bi, Te and InSb have been successfully electrodeposited[23] and this non-aqueous halometallate electrolyte system has been widely used to prepare binary and ternary materials. For example, bismuth telluride thin films were electrodeposited and the composition of these films was successfully controlled [37]. Thermoelectric properties of these films have also been examined [24]. Electrodeposition of germanium antimony telluride alloys and crystalline HgTe were investigated, the composition and morphology was adjusted by tuning the precursor concentrations and the electrodeposition conditions [38].

In this work, templated electrodeposition of bismuth, tellurium and bismuth-tellurium was carried out from the non-aqueous halometallate electrolyte system. Mesoporous silica thin films with *Fmmm* mesostructure coated on conductive Pt substrates were used as the templates for electrodeposition. To improve the adhesion between the Pt surface and the mesoporous silica films, (3-mercaptopropyl)trimethoxysilane was grafted on the Pt to form strong Pt-S chemical bonds and covalent $–C–Si–(OSi)_m(OH)_{3-m}$ bonds with the silica. To improve the permeation of halometallate salt solution in the mesopores, 3-chloropropyldimethyl methoxysilane was grafted on to the silica films to encourage the DCM electrolyte to wet the mesopores.

2. Experimental

2.1. Chemicals

98 % Tetraethoxysilane (TEOS) and 95 % (3-mercaptopropyl)trimethoxysilane (MPTMS) were obtained from Alfa Aesar. Triblock copolymer F127, 99 % tetrabutylammonium tetrafluoroborate [N^nBu_4][BF_4], ≥ 99.0 % tetrabutylammonium chloride ([N^nBu_4]Cl), 95 % dichloromethane (DCM) and 37 wt.% hydrochloric acid were from Sigma-Aldrich. Solvents 99.5 % isopropanol, 99 % dichloromethane, 99.8 % absolute ethanol and acetonitrile were from Fisher. 3-Chloropropyldimethyl methoxysilane was from Fluorochem. Deionised water (18 MΩ cm) was from a Suez Select Fusion ultrapure water deionisation unit. Pt substrates were made by sputtering 200 nm of Pt and 20 nm Ti onto a 700 mm thick silicon wafer. The Ti layer is to improve adhesion of Pt on the silicon wafer. The substrate size was 8×20 mm. Dichloromethane was stored in the nitrogen-purged glovebox after being dried and degassed by refluxing with CaH_2. The halometallate precursors [N^nBu_4][$BiCl_4$] and [N^nBu_4]$_2$[$TeCl_6$] were synthesised by previously published methods [23,39-42]. These chemicals were all stored in the glove box.

2.2. Modification of Pt substrates

Mesoporous silica films display poor adhesion on unmodified Pt substrates. Therefore, (3-mercaptopropyl)trimethoxysilane (MPTMS) was electrografted on Pt substrates to improve the adhesion between mesoporous silica films and Pt substrates. The electrografting process was conducted by scanning three consecutive cyclic voltammograms between 0 V and 1.8 V on Pt substrates in a solution of 2 mmol L^{-1} MPTMS and 100 mmol L^{-1} [N^nBu_4][BF_4] in acetonitrile at 200 mV s^{-1}, as shown in Fig. 1(a). The counter electrode and reference electrode were a Pt mesh and a steel rod respectively.

MPTMS binds to the Pt substrate via the thiol (–SH) functionality and its alkoxysilane moiety enables condensation with the mesoporous silica film. However, MPTMS can also block the Pt surfaces. Therefore, the electroactive probe [$Ru(NH_3)_6$]$^{3+/2+}$ was used to characterise the MPTMS-grafted Pt substrates. The aqueous solution includes 1 mmol L^{-1} [$Ru(NH_3)_6$]Cl_3 and 100 mmol L^{-1} $NaNO_3$. As shown in Fig. 1(b), three Pt substrates modified with 2 mmol L^{-1} MPTMS for 3, 5, 10 voltammogram cycles were characterised by cyclic voltammetry with probe [$Ru(NH_3)_6$]$^{3+/2+}$, an unmodified Pt substrate was measured for comparison. The current densities for [$Ru(NH_3)_6$]$^{3+}$ on Pt substrates modified for 3, 5, and 10 cycles are similar with the unmodified Pt substrate. It indicates that the MPTMS grafted-Pt substrates' surfaces are not blocked over a wide area after 10 voltammogram cycles grafting. In Fig. 1(b), the 3-cycles grafted Pt substrate shows highest current density, indicating it has the least surface coverage. This modified substrate also displays excellent adhesion between the Pt substrate and mesoporous silica film in the tape test. Therefore, 3-cycles grafting were used to modify the Pt substrates for supporting the mesoporous silica films.

2.3. Preparation of mesoporous silica films

The precursor solution was prepared using the method developed by Zhao et al. [33]. 1.0 g TEOS was dissolved into 5.64 g ethanol, 0.80 g deionised water and 0.10 g of 1 mol dm^{-3} hydrochloric acid at 338 K and stirred for 45 min. 0.3024 g Triblock copolymer F127 was dissolved into 5.64 g ethanol. The precursor solution was prepared by mixing these two solutions and stirring at room temperature for 60 min. Pt substrates were cleaned with isopropanol then deionised water by ultrasonication and were dried with a nitrogen jet. Dip-coating was used to coat the silica films onto the modified Pt substrates. The cleaned and modified Pt substrates were vertically immersed into the prepared precursor solution and withdrawn at 150 mm min^{-1} under 75 % relative humidity at 298 K. The as-made films were aged at 120 °C for 10 h. The
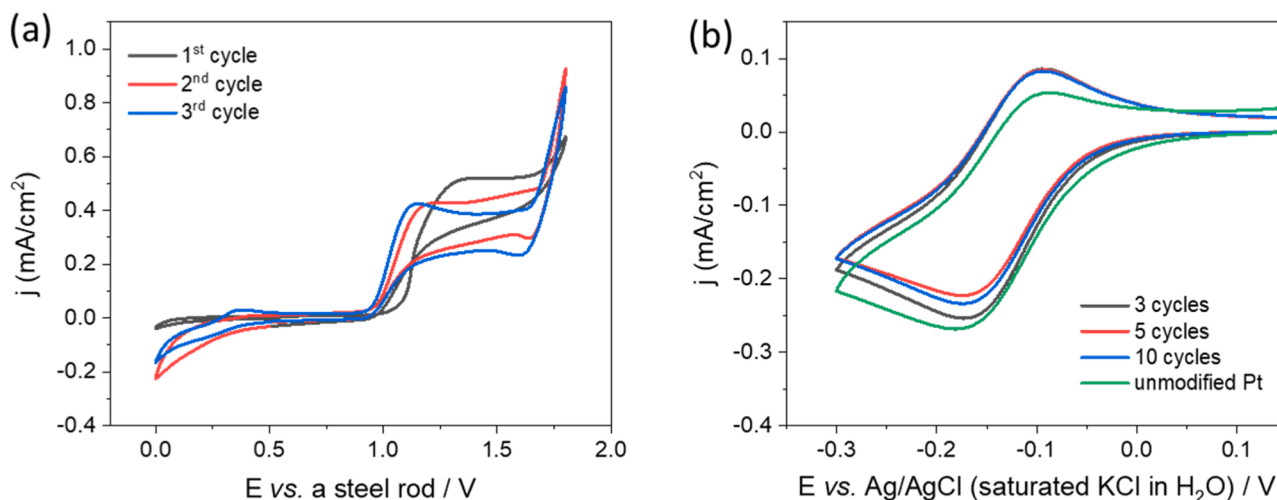
Fig. 1. (a) Three consecutive cyclic voltammograms of a bare Pt substrate in the electrografting solution of 2 mmol L^{-1} MPTMS and 100 mmol L^{-1} $[N^nBu_4][BF_4]$ in acetonitrile at 20 mV s^{-1}. The reactive area was controlled by the front seal cell as 12.56 mm^2. Counter electrode (CE): a Pt mesh; Reference electrode (RE): a steel rod; Working electrode (WE): Pt substrates. (b) Cyclic voltammograms of 1 mmol L^{-1} $[Ru(NH_3)_6]Cl_3$ and 100 mmol L^{-1} $NaNO_3$ in aqueous solution. The potential scan rate was 20 mV s^{-1}. The reaction area is 12.56 mm^2. CE: a Pt mesh; RE: a homemade Ag/AgCl electrode (saturated KCL inH_2O); WE: MPTMS grafted Pt substrates and an unmodified Pt substrate.

surfactant F127 was removed by bathing the films in the DCM solution for 4 h and calcined in air at 350 °C for 5 h after ramping of the temperature at a rate of 1 °C min^{-1}. As reported in our previous study using the same silica production method, the as-made mesoporous silica films are highly ordered with pore diameters of 6–10 nm and the thickness of films are between 100 and 200 nm [29]. The mesostructure displays the *Fmmm* unit cell structure with the [0 1 0] axis perpendicular to the substrate.

3-Chloropropyldimethyl methoxysilane was grafted to the prepared mesoporous silica films coated on Pt substrates. Its Si–O–CH_3 groups anchor to the mesoporous silica surface through forming Si–O–Si bonds and its chloro-substituent groups allow DCM solutions to wet the surface and hence the chlorometallate salts in the electrolyte to go into the mesopores. This procedure needs to be conducted under anhydrous conditions as the silane reacts with water. First, the samples and the glassware were dried under vacuum overnight at 120 °C. After cooling the glassware to room temperature and flushing N_2 into the closed glassware, 40 ml dry toluene and 1.8 ml of 3-chloropropyldimethyl methoxysilane were injected into the glass tube to avoid including any moisture from the air. The synthesis was carried out at 65 °C for 24 h. Finally, the mesoporous silica films on Pt substrates were washed twice with dried toluene, twice with DCM, and twice with absolute ethanol under sonication. The samples were then dried under vacuum at 120 °C overnight. After grafting and cleaning, the samples were stored in the nitrogen-purged glovebox before conducting electrochemistry.

2.4. Electrodeposition

All cyclic voltammetry and electrodeposition experiments were performed in a three-electrode system with a Metrohm EcoChemie Autolab PGST AT100 potentiostat/galvanostat, controlled by NOVA 1.10 software in a nitrogen-purged recirculating glove box (Belle Technology). Before being used as the templates for electrodeposition, MPTMS grafted-Pt substrates coated with mesoporous silica films were dried at 120 °C under vacuum overnight to remove the moisture in the pores. Electrolyte solutions for Te or Bi electrodeposition were 100 mmol L^{-1} $[N^nBu_4]Cl$, and either 10 mmol L^{-1} $[N^nBu_4]_2[TeCl_6]$ or 5 mmol L^{-1} $[N^nBu_4][BiCl_4]$ dissolved in 10 mL anhydrous CH_2Cl_2. Bismuth-tellurium electrodeposition used 100 mmol L^{-1} $[N^nBu_4]Cl$, 2.25 or 3 mmol L^{-1} $[N^nBu_4][BiCl_4]$ and 3 mmol L^{-1} $[N^nBu_4]_2[TeCl_6]$ in 10 mL anhydrous CH_2Cl_2. The working electrodes were Pt substrates

coated with mesoporous silica films after MPTMS was grafted to the Pt surface. A home-made Ag/AgCl electrode (0.1 M $[N^nBu_4]Cl$ in anhydrous CH_2Cl_2) and a platinum disk were used as the reference and counter electrodes, respectively. The three electrodes were sealed into a specially designed one-compartment electrochemical cell within a wire mesh Faraday cage. The reactive area was controlled as a circle with diameter of 4 mm, thus the reaction area was 12.56 mm^2.

2.5. Characterisation

The SEM images were collected with a ZEISS Sigma 500 VP FE-SEM with an Oxford Instruments Ultim 170 energy-dispersive X-ray (EDX) detector. High resolution X-ray diffraction patterns were obtained using a Rigaku Smartlab over the 2θ angle region from 10° to 90°.

3. Results and discussion

3.1. Electrochemistry

Cyclic voltammetry (CV) was used to study the initial stages of electrodeposition from the halometallate electrolyte system. Fig. 2 shows typical results for the voltammetry of $[N^nBu_4][BiCl_4]$ and $[N^nBu_4]_2[TeCl_6]$ separately and then together in DCM solution with $[N^nBu_4]Cl$ electrolyte (replicate voltammograms are shown in Figure S1). Results for both bare Pt and mesoporous silica coated Pt electrodes are shown for comparison.

Electrochemistry on bare Pt. We begin by considering the results on the bare Pt electrodes, Fig. 2(a), (c) and (e). For the $[N^nBu_4][BiCl_4]$ (Fig. 2(a)) two reduction peaks were observed at −0.72 V and −1.60 V on the first cycle, whereas only one reduction peak was observed around −0.75 V on the second and the third cycles. These results agree with those reported previously for this system [23] with Bi(III) being reduced to Bi. For $[N^nBu_4]_2[TeCl_6]$ (Fig. 2(c)) the potential was initially scanned from 0.4 V to −1.0 V and then between −1.0 V and 1.0 V for three cycles. On the first scan, the deposition started at around −0.25 V and increased gradually to a peak at −0.77 V. Two stripping peaks are seen on the reverse scan. On the second and third scans, the reduction peaks shifted to significantly to more positive potential because of the presence of Te on the electrode surface. After three scans, the Pt electrode was covered by a visible black film. These results are consistent with our previous work on Te electrodeposition from $[N^nBu_4]_2[TeCl_6]$ where a full

On bare Pt

On silica film coated Pt
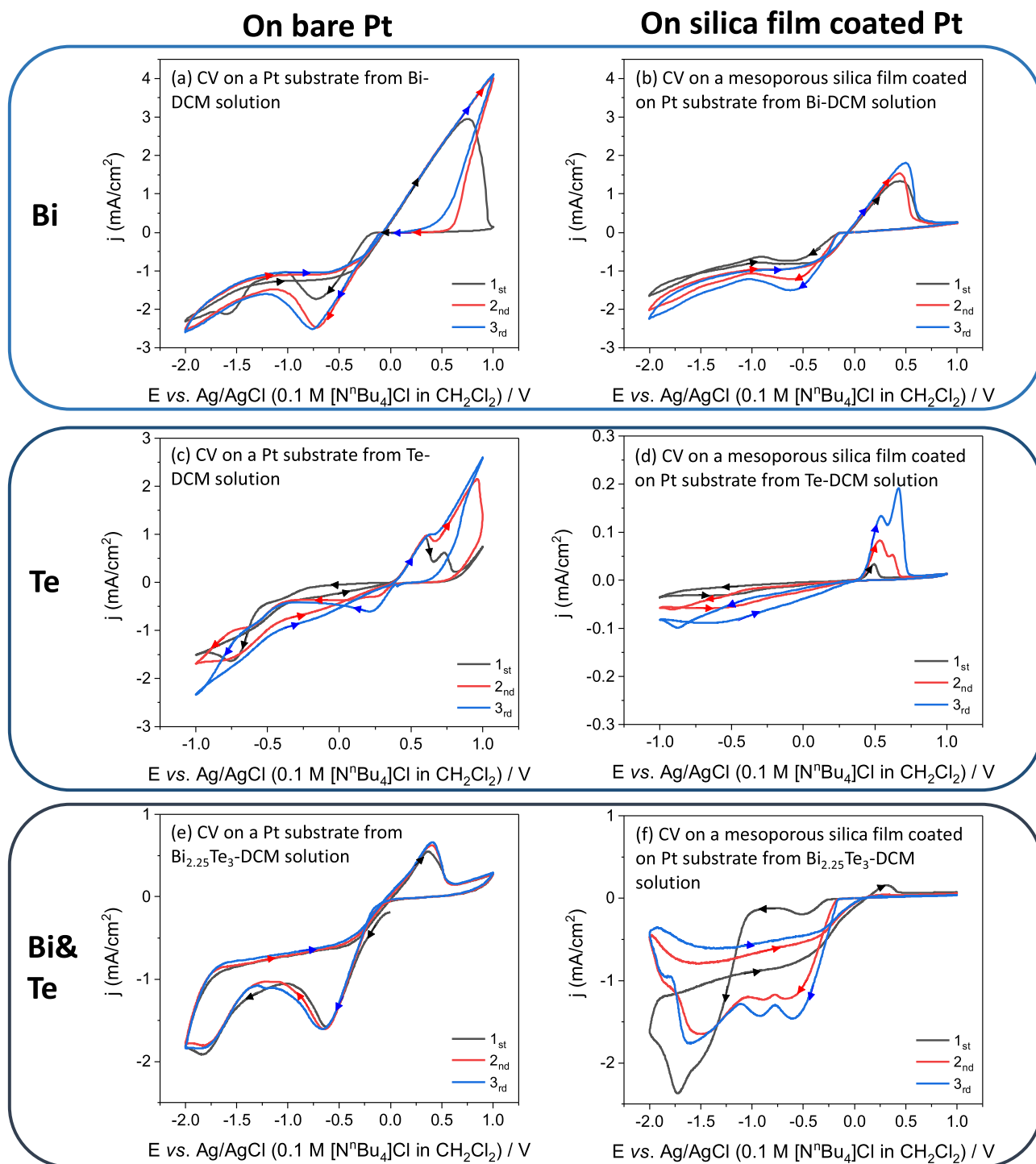
Fig. 2. Cyclic voltammograms of (a, b) 5 mmol L^{-1} $[N^nBu_4][BiCl_4]$, (c, d) 10 mmol L^{-1} $[N^nBu_4]_2[TeCl_6]$ and (e, f) 2.25 mmol L^{-1} $[N^nBu_4]_2[BiCl_4]$ and 3 mmol L^{-1} $[N^nBu_4]_2[TeCl_6]$ in anhydrous CH_2Cl_2 containing 100 mmol L^{-1} $[N^nBu_4]Cl$ as the supporting electrolyte on a bare Pt substrate and a mesoporous silica film coated on Pt substrate. The potential scan rate was 50 mV s^{-1}. The reaction area is 12.56 mm^2. CE: a Pt disk; RE: a homemade Ag/AgCl electrode (0.1 M $[N^nBu_4]Cl$ in anhydrous CH_2Cl_2); WE: Pt substrates or mesoporous silica film-covered Pt substrates.

discussion of the mechanism can be found [43]. In that work it was shown that there is a large overpotential (>1 V) to deposition of Te on the first reduction scan at clean Pt electrodes because of the thermodynamic barrier to the initial reduction of Te(IV) to Te(III) but this was not evident for the electrodeposition of Te onto a Te coated electrode. To account for this a catalytic mechanism involving the formation of a Lewis acid-base adduct between the Lewis acidic $[TeCl_5]^-$ ion and the Lewis basic tellurium (0) surface was proposed. This was shown to be

consistent with the results of DFT calculations for the speciation equilibria for the Te(IV) chloride complexes and the results of experiments at different chloride concentrations [43].

In the case of the mixture of $[N^nBu_4][BiCl_4]$ and $[N^nBu_4]_2[TeCl_6]$ (Fig. 2(e)) the potential was initially scanned from 0 V to -2.0 V and scanned between -2.0 V and 1.0 V for the second and third cycles. All three scans show similar features with two pronounced reduction peaks at -0.65 V and -1.80 V. This voltammetry is consistent with previous

work on TiN electrodes [44] where bismuth telluride was shown to be deposited between −0.6 and −2.0 V vs. Ag/AgCl, with the composition being essentially independent of the potential but controlled by the ratio of Bi to Te concentration in the solution.

Electrochemistry on mesoporous silica coated Pt. Turning our attention to the deposition through the mesoporous silica we can see that for [N^{n}Bu$_4$][BiCl$_4$] (Fig. 2(b)) the results are almost identical to those on bare Pt (Fig. 2(a)) except that the current density, based on the geometric area of the electrode, is about 25 % lower. This is consistent with the reduction of the exposed Pt surface area due to the presence of the mesoporous silica combined with a possibly slower rate of diffusion through the 8 nm pores of the mesoporous film. However, the fact that the voltammetry and current densities are so similar clearly indicates that a large number of mesopores are accessible and the silica film is a suitable template for bismuth electrodeposition.

In contrast the voltammetry of [N^{n}Bu$_4$]$_2$[TeCl$_6$] at the mesoporous silica coated electrode (Fig. 2(d)) shows significant differences from the behaviour at bare Pt (Fig. 2(c)) and the current density is an order of magnitude smaller. There is clearly still some electrodeposition of Te as shown by the pair of stripping peaks at 0.54 and 0.67 V (in the third scan) but reduction peaks are drawn out and much less distinct with the current gradually increasing on the first negative scan from the starting potential at 0.4 V. After three scans, the mesoporous silica coated Pt electrode was covered by a visible black film due to Te deposition. An obvious explanation for the reduced current density for Te deposition on the mesoporous silica could be that in this case the pores were blocked by unremoved surfactant from the preparation of for some other reason. However, this is not the case. Figure S1 in the SI shows results for a number of replicate experiments at bare Pt and mesoporous silica coated Pt electrodes. For each electrolyte solution, one replicate experiment was recorded on bare Pt and two replicate experiments were carried out for the mesoporous silica coated Pt electrodes. All the mesoporous silica films used for Bi, Te and Bi-Te voltammetry were prepared at the same time following the same procedure and the voltammetry was carried out in the glove box on the same day. Fig. 2(d) and Figures S1(e) and S1(f) show that voltammetry of the Te solution on the mesoporous silica coated electrodes is consistent and the current is always an order of magnitude lower than for the Bi and Bi-Te cases, showing that the low current is not caused by blocked mesopores either due to unremoved surfactant or due to some interaction of the [TeCl$_6$]$^{2-}$ with the pore walls. This suggests that the reduction in current density is a consequence of the effect of confined diffusion within the pores on the Te electrodeposition reaction presumably caused by the effect of the build-up in chloride concentration at the electrode surface on the tellurium speciation.

For the voltammetry of the [N^{n}Bu$_4$][BiCl$_4$] and [N^{n}Bu$_4$]$_2$[TeCl$_6$] mixture on the mesoporous silica coated Pt (Fig. 2(f)) the current densities are comparable to those on the bare Pt, confirming that the pores are not blocked, but the shape of the voltammograms are different (compare to Fig. 2(e)). On the first scan, after a small reduction peak at −0.5 V, the current increases steeply from −0.96 V reaching a reduction peak at −1.73 V. On the return scan the current is now larger until the relatively small, compared to the charge passed for reduction, stripping peak at 0.31 V. On the second and the third scans, the reduction currents are larger and increase from −0.25 V finally reaching a peak at −1.5 V. The stripping peaks are now even smaller. The same behaviour can be seen in the replicates (Figure S1(h) and (i)).

We know from studies of mesoporous films in aqueous solution that the charge on the redox species can affect the permeability for anionic complexes such as [Fe(CN)$_6$]$^{3-/4-}$ being much lower than that for neutral or cationic complexes due to the surface negative charge on the silica. However, we do not believe this is the cause in the present case because the modification of the mesoporous silica with 3-chloropropyldimethyl methoxysilane, used here to improve wetting with CH$_2$Cl$_2$, will have modified the surface -OH groups and significantly reduced the surface charge on the silica. In addition, both reactive species used in the

electrodeposition, [BiCl$_4$]$^-$ and [TeCl$_5$]$^-$, are anions and of similar size so should be affected very similarly. The differences in the voltammetry for the Bi/Te on the bare Pt and mesoporous silica coated Pt again suggest that this is caused by the effect of confined diffusion on the Te speciation due to the build-up in chloride concentration at the electrode surface during electrodeposition since we know from our previous work (and the results in Fig. 2) that the electrodeposition of Bi from [N^{n}Bu$_4$][BiCl$_4$] in DCM is rather well behaved [23], whereas the deposition of Te from [N^{n}Bu$_4$]$_2$[TeCl$_6$] in DCM is a very complex process and affected by Cl$^-$ concentration [43]. The differences in the voltammetry for the Bi/Te on the bare Pt and mesoporous silica coated Pt again suggest that this is caused by the effect of confined diffusion on the Te speciation due to the build-up in chloride concentration at the electrode surface during electrodeposition.

3.2. Electrodeposition experiments

Ideally, to electrodeposit materials uniformly into 3D mesoporous channels, nuclei need to form simultaneously at the bottom of as many of the pore channels in the mesoporous silica film template as possible, and then grow at the same rate to avoid faster deposition in regions where deposits have already grown closer to the template/electrolyte interface. Therefore, a pulsed electrodeposition method was used to rapidly form a large number of nuclei and then to grow these more slowly to maximise the likelihood of uniform growth through the pore channels, avoiding diffusion control [9,20]. This approach was used in our previous work on electrodeposition of gold into mesoporous silica [29]. A schematic of the pulsed electrodeposition procedure is shown in Figure S2. It starts with a short potential pulse (0.1 to 3 s) to a more negative potential to create nuclei. Then, after a 10 s rest time at 0.0 V, growth pulses (0.8 to 1 s) to less negative potentials were applied to grow the deposit. There is a pulse-off time of 10 s between each deposition pulse to allow the relaxation of the concentration of the precursor species in the pores. A variety of electrodeposition conditions were applied for Bi, Te and Bi-Te templated electrodeposition. Table 1 gives

Table 1
The applied conditions for pulsed electrodeposition and the transferred charge calculated from the current transient.

Sample	Electrolyte	Nucleation conditions	Growth conditions	Charge / C
Bi-1	Bismuth	−1.5 V, 2 s	−0.35 V, 1 s; 500 cycles	−0.078
Bi-2	Bismuth	−2.0 V, 3 s	−0.40 V, 1 s; 500 cycles	−0.020
Bi-3	Bismuth	−1.5 V, 1 s	−0.25 V, 1 s; 500 cycles	−0.045
Bi-4	Bismuth	−2.0 V, 3 s	−0.6 V, 1 s; 500 cycles	−0.037
Te-1	Tellurium	−2.0 V, 1 s	−0.50 V, 1 s; 1000 cycles	−0.044
Te-2	Tellurium	−2.0 V, 1 s	−0.70 V, 1 s; 850 cycles	−0.240
Te-3	Tellurium	−1.5 V, 0.1 s	−0.60 V, 0.8 s; 600 cycles	−0.010
Te-4	Tellurium	−1.5 V, 1 s	−0.80 V, 1 s; 850 cycles	−0.062
Te-5	Tellurium	−2.0 V, 1 s	−0.80 V, 1 s; 850 cycles	−0.190
BiTe-1	Bismuth, tellurium	−1.5 V, 1 s	−0.60 V, 1 s; 500 cycles	−0.261
BiTe-2	Bismuth, tellurium	−1.5 V, 3 s	−0.60 V, 1 s; 500 cycles	−0.195
BiTe-3	Bismuth, tellurium	−2.0 V, 1 s	−0.35 V, 1 s; 500 cycles	−0.085
BiTe-4	Bismuth, tellurium	−2.0 V, 3 s	−0.50 V, 0.8 s; 500 cycles	−0.150

*All the potentials in Table 1 are relative to Ag/AgCl (0.1 M [N^{n}Bu$_4$]Cl in CH$_2$Cl$_2$).

details of the electrodeposition conditions. Current-time plots for the first 100 pulsed electrodeposition potential sequences for typical samples are shown in Figure S3.

Bi and Te electrodeposition. A variety of electrodeposition conditions were applied to deposit Bi and Te into the mesoporous silica films. Figs. 3 and 4 show the top-view and cross sectional FE-SEM images of four typical samples at different magnifications. For the Bi electrodeposition samples, a few microsize/nanosize particles are observed on the surface of the film, indicating that most of the deposited Bi is within the film. The top-view SEM images of other bismuth deposition samples (Bi-3 and Bi-4) in Figure S4 display a similar surface morphology to the typical samples Bi-1 and Bi-2. Under high magnification ($100,000 \times$) the mesoporous silica film shows a highly ordered and crack-free surface with the mesopore size of around 8 nm. There are a few nanodots observed in the mesopores, these are likely to be deposited Bi that has reached the surface. When applying a more negative nucleation potential (-2.0 V for 3 s), more nanoparticles were found on the surface and more Bi features were also observed in the mesopores.

Te electrodeposition samples display more particles and aggregations on the surface of the film compared to the Bi electrodeposition samples. The smaller surface structures comprise chains of nanoparticles, as shown in Fig. 3 Te-1. Under high magnification ($100,000 \times$) some further growth was observed in the mesopores. There are large particle aggregations seen for Te-2, indicating that further particles tend to grow on the particles on the surface rather than in the mesopores. The size of the growths in the pores in Te-2 are the same as the diameter of the mesopores, which indicates that the Te nanoparticles are growing in the pores. Figure S5 shows top-view FE-SEM images of Te-3,4,5, which display similar surface features.

The cross-section FE-SEM images in Fig. 4 show that there are a few Te nanowires grown through the pores and just beyond the surface. The crystal structure of tellurium comprises spiral chains of bonded Te atoms packed in a hexagonal array and, as a consequence Te often shows 1D growth [45]. For both samples, even though only a small fraction of the mesopores have wires growing out to the surface, the observation of nanowires is significant as it shows the possibility of fabricating sub-10 nm nanowires through templated electrodeposition.

The structures of the electrodeposited materials were investigated using XRD. All the bismuth and tellurium electrodeposition samples showed similar XRD patterns. Typical XRD patterns of bismuth and tellurium deposited in mesoporous silica films are shown in Fig. 5, together with diffraction patterns for the mesoporous silica film coated Pt substrate (red) and standard hexagonal bismuth ICSD-64703 and trigonal tellurium ICSD-65692 patterns (green). In Fig. 5(a), the reflections for the Bi deposit match well with the hexagonal bismuth [46]. The 0 0 3, 1 0 1, 0 1 2, 1 0 4 and 1 1 0 peaks are observed at $22.5°$, $23.7°$, $27.3°$, $37.8°$ and $39.2°$, respectively. Other peaks are identified in Fig. 5 (a). The sharp peak at $52.6°$ originates from the silicon wafer of the Pt substrate. The broad feature between $10°$ to $20°$ arises from the mesoporous silica film. Compared to the silica film on the Pt substrate, the peak of the silicon wafer for the Bi in mesoporous silica film shifts to a slightly lower angle. This is likely to be a result of a small sample alignment error. The peaks at $40.1°$, $46.6°$, $67.8°$ and $81.8°$ correspond to the 1 1 1, 0 2 0, 2 2 0 and 1 1 3 peaks of the face-centred cubic Pt structure (ICSD-243678). The XRD pattern indicates that Bi has been electrodeposited successfully. In Fig. 5(b), the 1 0 0, 1 0 1, 1 0 2, 1 1 0, 1 1 1, 0 0 3 and 0 2 1 reflections of trigonal tellurium are observed at $23.0°$, $27.5°$, $38.3°$, $40.4°$, $43.6°$, $46.4°$ and $49.5°$, respectively [47]. The tellurium 1 1 0 and 0 0 3 peaks overlap with the Pt 1 1 1 and 0 2 0. The XRD pattern shows the presence of Te. The EDS mapping images in (c-f) prove that the deposited particles on the film are Bi and Te.

Bi-Te codeposition. As there are two species involved and three reduction peaks observed in the CV (Fig. 2(f)), a wide range of deposition conditions were applied to conduct the pulsed electrodeposition on mesoporous silica films coated on Pt substrates. The top-view SEM images in Fig. 6 show the morphologies of the deposits in and on the

mesoporous silica films. The details of the deposition conditions are labelled in each image. For each sample, the images collected at $1000 \times$ and $200,000 \times$ magnification are displayed. In $1000 \times$ images, there are micro-size bulk particle aggregations at the surface of thin films for all samples. The highly ordered mesopores can be seen in the high magnification ($200,000 \times$) images. There are a few small features seen in the mesopores, in particular for the sample with longer nucleation times, the SEM images of BiTe-2 and BiTe-3 show deposited nanoparticles emerging from the mesopores. The observation of deposition in individual mesopores is significant as it shows the conditions used result in electrodeposition through the pores.

In our previous work, HF evaporation was used to etch mesoporous silica film away so to observe the deposits better [29]. It has been observed that the deposits' size of most particles are bigger than the templated mesopore sizes, but the mesopore sizes can still affect the deposit particle sizes [29]. In this work, it was found that HF can etch the deposited Bi, Te Bi-Te nanoparticles away, only bulk materials left after HF etching. Therefore, HF etching was not adopted. The top-view SEM images (Figs. 3 and 6) show that the particle sizes on the surface have a wide distribution. There are small nanoparticles in the mesopores, nanoparticles covered mesopores and bulk aggregations. It indicates that the deposits unevenly growing in the mesopores.

As shown in Fig. 7, XRD along with EDX were conducted to investigate the crystalline structure and chemical composition of the bismuth-tellurium deposited in the mesoporous silica films under different pulsed conditions. The XRD patterns of the samples deposited under different conditions are all similar. They are all indexed to tellurium (ICSD-65692). The sharp peak at $52.6°$ comes from the silicon wafer of the Pt substrate and the strong peak at $67.8°$ is attributed to the Pt 0 2 0 reflection. Other peaks are attributed to trigonal tellurium. The thickness of the mesoporous silica films is about 120 nm [29]. EDX was conducted with an electron acceleration of 15 kV, corresponding to a penetration depth of about 1 μm. Thus, EDX is able to give information over the electrodeposition area. There is very low bismuth content detected in all the samples, and this is consistent with the XRD patterns. Fig. 7(b) shows the EDX mapping of BiTe-2. It is proposed that the electrodeposited particles are bismuth-doped tellurium.

Compared to the deposition of bismuth or tellurium on its own, electrodeposition of bismuth-tellurium here generally gives higher currents and hence greater charge passed. The cyclic voltammetry current for $[N^nBu_4]_2[TeCl_6]$ in Fig. 2(d) is >10 times lower than that of electrolyte containing Bi and Te in Fig. 2(f). The deposition current for Te electrodeposition is low, while on mixing Bi and Te in the electrolyte, the current increases significantly even though the resulting electrodeposit is mainly Te. Using the same non-aqueous halometallate electrolyte system and the similar electrodeposition conditions, previous work has successfully electrodeposited Bi_2Te_3 on bare TiN substrates [23-24]. However, here when using mesoporous silica templates on Pt, the deposits are very Te rich by EDX and show trigonal tellurium structure by XRD. To try to understand this paradox further experiments were carried out varying the deposition conditions and comparing the bare Pt and mesoporous silica coated Pt electrodes. Details of the experimental conditions are given in Table 2. A variety of pulsed electrodeposition conditions were applied on bare Pt substrates for comparison, the effect of deposition time was investigated, and the concentration of $[N^nBu_4]$ $[BiCl_4]$ was increased since it has been reported that upon increasing the concentration from 2 to 3 mmol L^{-1} the deposit composition changed from $BiTe_2$ (33 ± 3 % Bi) to Bi_4Te_3 (55 ± 5 % Bi) [44]. The bismuth and tellurium atomic percentage ratios calculated from EDX of each samples are listed in Table 2.

XRD patterns in Fig. 8(a) show the deposits on the bare Pt substrates display the same trigonal tellurium. EDX of BiTe-Pt-1 and 2 show that the Bi content is again very low and are similar to the deposits in the mesoporous silica films. These results indicate that the low Bi content is not caused by the effect of confinement in the mesopore channels. However, when conducting potentiostatic electrodeposition, BiTe-Pt-4
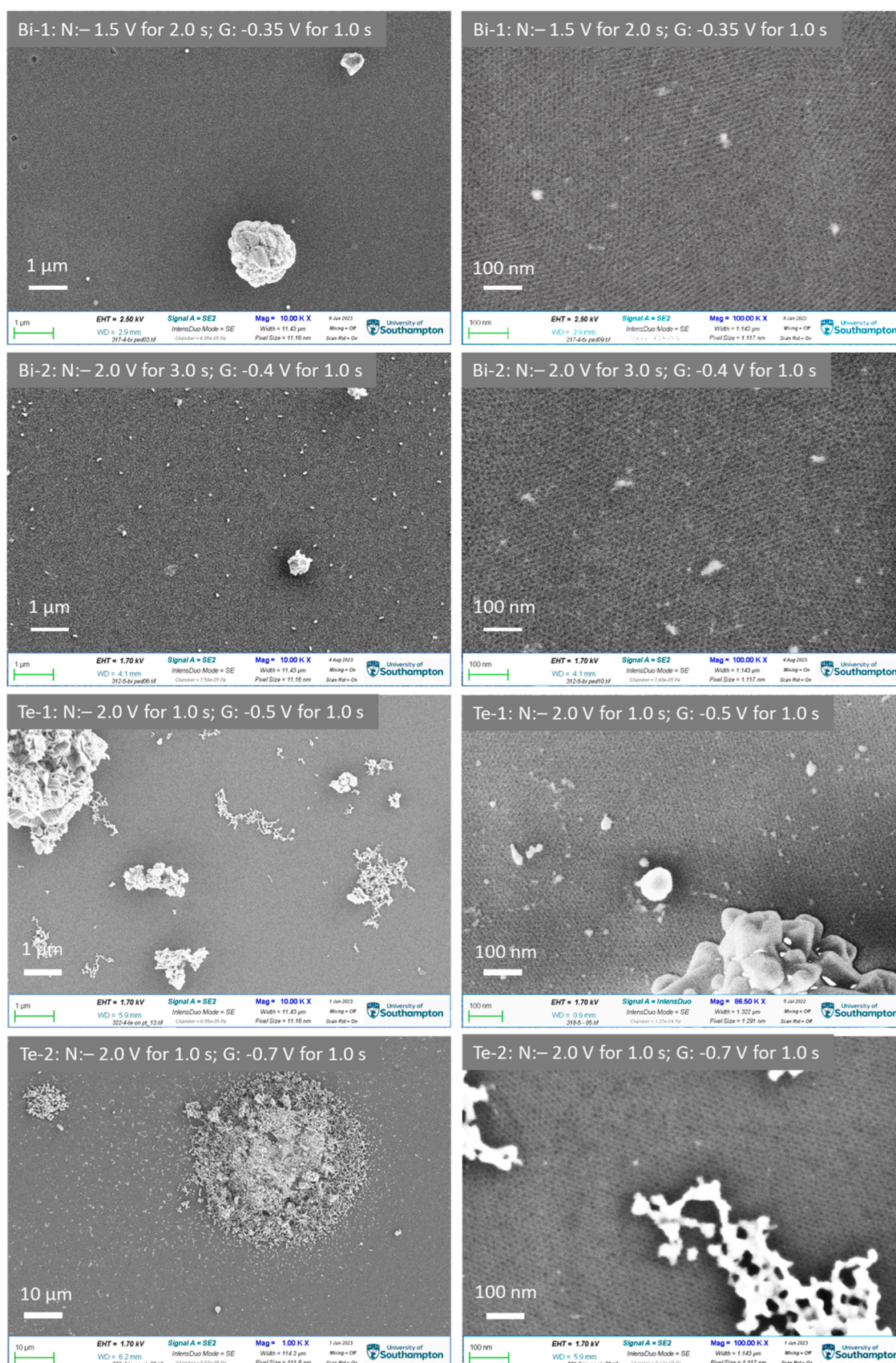
Fig. 3. Top-view FE-SEM images of Bi and Te electrodeposited in the mesoporous silica films with different nucleation and pulsed growth potentials. The electrodeposition conditions are labelled in each image.
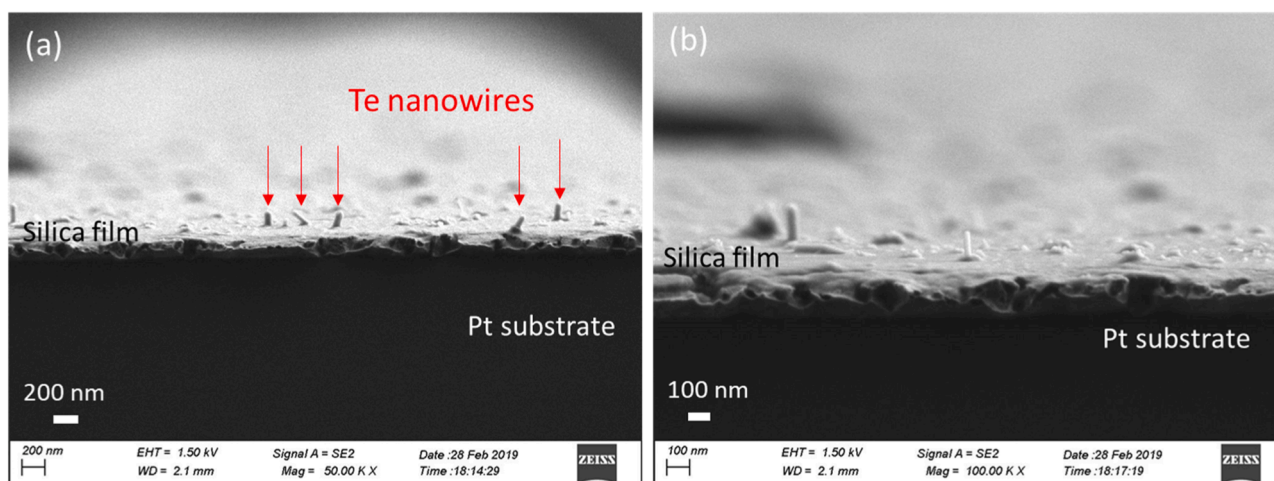
Fig. 4. Cross section SEM images of Te electrodeposited in the mesoporous silica films.
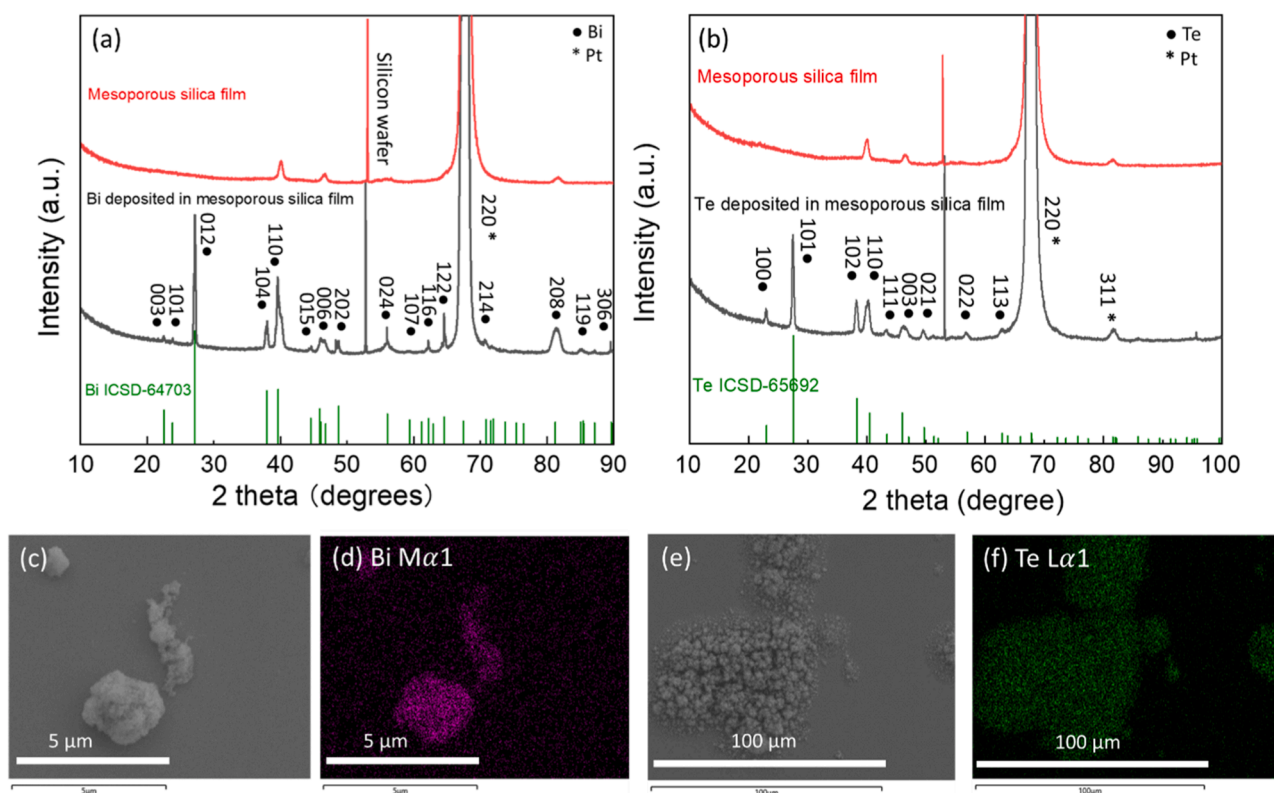

Fig. 5. (a,b) XRD patterns collected for the mesoporous silica film (red) and bismuth or tellurium deposited in the mesoporous silica film (black). The patterns at the bottom of the figure are the standard intensities for hexagonal bismuth ICSD-64703 and tellurium ICSD-65692 XRD (green), and the key reflections are labelled; (c-f) The EDS mapping of the Bi and Te electrodeposited on mesoporous silica films.

displays the expected, much higher, Bi:Te ratio of 0.36:1 although the XRD pattern still shows the presence of trigonal tellurium.

For BiTe-5 and BiTe-6, Fig. 8(b), longer pulse times (5 s per deposition pulse) and potentiostatic growth were used to deposit bismuth-tellurium in the mesoporous silica films. For the 5 s pulses, BiTe-5 still shows very high Te content by EDX. However, potentiostatic deposition through mesoporous silica, sample BiTe-6, shows higher bismuth content (Bi:Te = 0.49:1), close to the Bi_2Te_3 composition (Bi:Te = 0.67:1). However, the XRD pattern still shows the presence of trigonal tellurium. The peaks at 23.0°, 27.5°, 38.3°, 40.4°, 43.6°, 46.4°, 49.5°, 57°, 62.9°, 66.0°, 72.7° are identified as the 100, 101, 102, 110, 111, 003, 021, 022, 113, 231 and 232 reflections of trigonal tellurium (ICSD 65692). The

Bi_2Te_3 pattern generally has obvious peaks at 17.5°, 27.8°, 37.9°, 41.1°, 44.7°, 50.5°, 57.1°, 62.3°, 66.8° and 72.7° [48]. Ordered Bi_2Te_3 nanowire arrays have a strong peak at 40°, corresponding to the (110) plane [49]. A few peaks of Te and Bi_2Te_3 are at similar positions. Figure S6 compares the XRD patterns of BiTe-2 and BiTe-6 with Te (ICSD-65692) and Bi_2Te_3 (ICSD-7743) standard patterns. It is obvious that BiTe-2 and BiTe-6 are Te phase. The diagnostic peaks of Bi_2Te_3 are at 17.5°, 37.9° and 41.1°. There are no peaks observed at around 17.5° in the deposited samples. The positions and intensities of peaks between 37° and 57° suggest they belong to Te phase. Therefore, the obtained BiTe-6 deposits have the trigonal Te structure even though EDX shows a high Bi content.

Note that XRD patterns for the different bismuth-tellurium
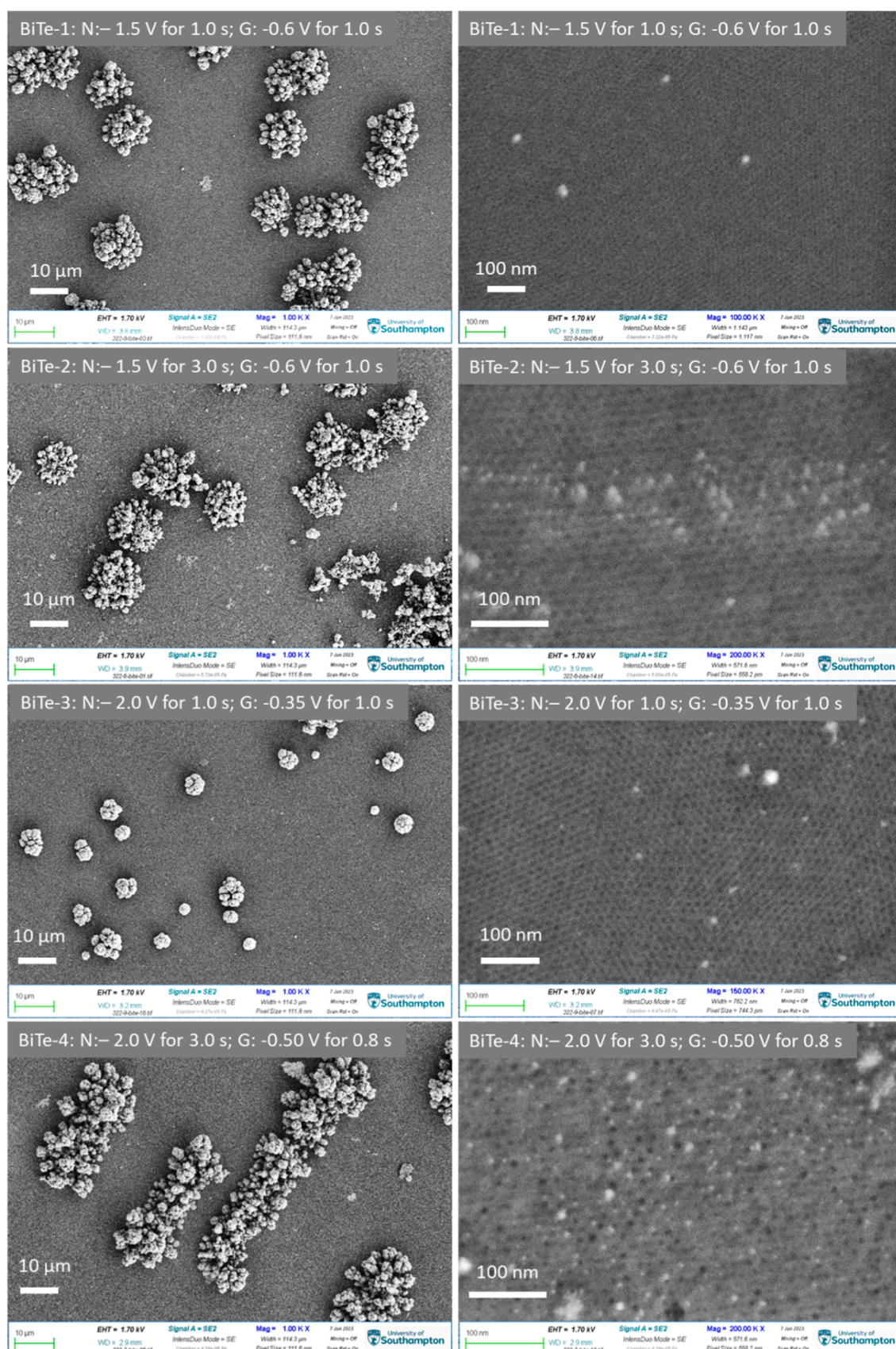
Fig. 6. Top-view SEM images of bismuth-tellurium electrodeposited in the mesoporous silica films with different nucleation and pulsed growth potentials. The electrodeposition conditions are labelled in each image.
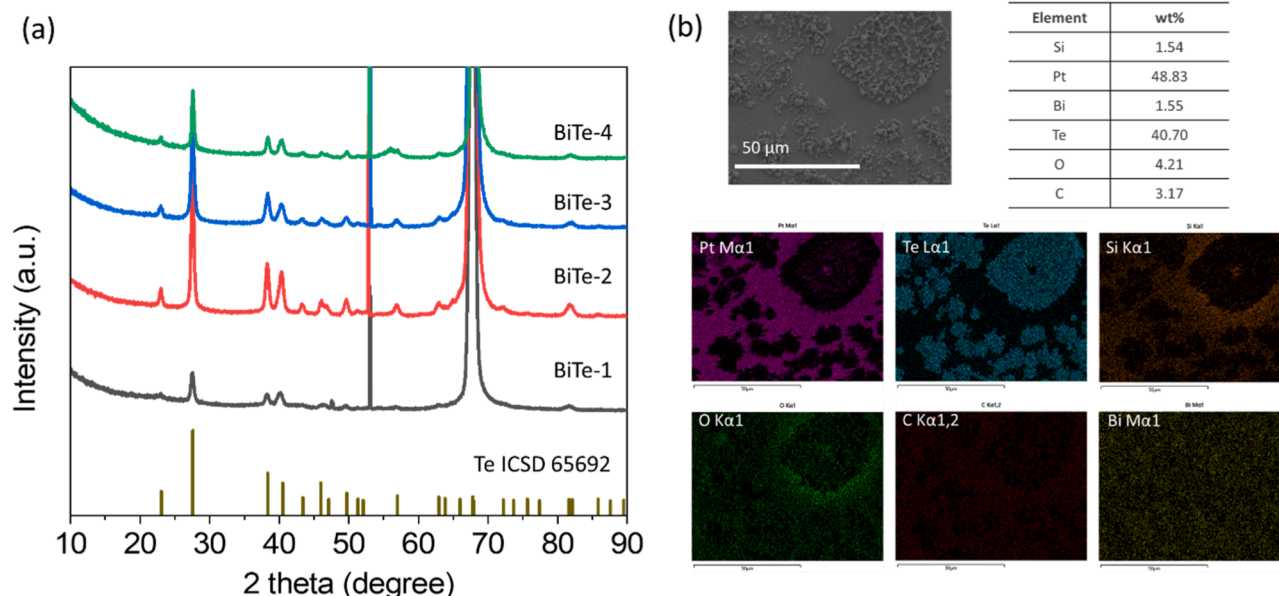
Fig. 7. (a) XRD patterns of bismuth telluride deposited in the mesoporous silica film with different electrodeposition conditions. (b) The EDS mapping of BiTe-2.

Table 2

The table of bismuth concentration in electrolyte, electrodeposition conditions and the bismuth and tellurium atomic percentage ratios calculated from EDX. 3 mmol L^{-1} [N^{n}Bu$_4$]$_2$[TeCl$_6$] and 2.25/3 mmol L^{-1} [N^{n}Bu$_4$][BiCl$_4$] were dissolved in 10 mL anhydrous CH$_2$Cl$_2$ containing 100 mmol L^{-1} [N^{n}Bu$_4$]Cl as the electrolyte.

Sample No.	Bi / mmol L^{-1} concentration	Nucleation conditions	Growth conditions	Bi: Te (at %: at%)
BiTe-Pt-1	2.25	−2.0 V, 0.5 s	−0.60 V, 1.0 s; 50 cycles	0.02 ±0.01:1
BiTe-Pt-2	2.25	−1.5 V, 0.5 s	−0.60 V, 1.0 s; 50 cycles	0.03 ±0.01:1
BiTe-Pt-3	2.25	−1.5 V, 3.0 s	−0.60 V, 1.0 s; 50 cycles	–
BiTe-Pt-4	2.25	–	−1 V, 10 min	0.36 ±0.03:1
BiTe-5	2.25	−1.4 V, 5.0 s	−0.60 V, 5.0 s; 200 cycles	0.02 ±0.01:1
BiTe-6	2.25	−1.4 V, 5.0 s	−0.60 V, 5.0 min;	0.49 ±0.01:1
BiTe-7	3.00	−1.5 V, 1.0 s	−0.25 V, 0.8 s; 1000 cycles	0.02 ±0.01:1
BiTe-8	3.00	−2.0 V, 1.0 s	−0.25 V, 0.8 s; 1000 cycles	0.02 ±0.01:1

*All the potentials in Table 2 are relative to Ag/AgCl (0.1 M [N^{n}Bu$_4$]Cl in CH$_2$Cl$_2$).

compounds share many reflection positions because their structures are strongly related [37] and this makes unequivocal assignment difficult. The standard patterns of other common bismuth-tellurium compounds including Bi$_3$Te$_4$, BiTe, Bi$_4$Te$_5$ were also compared but they do not match with the pattern observed. For example, BiTe (ICSD 7742) has prominent peaks at 27.8°, 38.2°, 41.2° and 50.5° [48]. Bi$_4$Te$_3$ (ICSD 7747) shows obvious peaks at 27.5°, 37.8°, 40.8° and 49.9° [48]. These main peak positions are similar to those found with Te and Bi$_3$Te$_4$. However, the peaks at around 18.5° and 23.7° do not match with diffraction patterns of BiTe-6 here. As a result, it is thought that potentiostatic electrodeposition produced a deposit of tellurium doped by a high ratio of bismuth.

For BiTe-7 and 8, Fig. 8(c), bismuth-tellurium was electrodeposited in the mesoporous silica film coated on Pt substrates from the electrolyte with higher bismuth concentration. The deposits also have low Bi content from EDX and their XRD patterns match well with Te ICSD 65,692.

In summary, when conducting pulsed electrodeposition in Bi-Te electrolyte solution, the composition of the deposited materials was found to be independent of the potential over the range from −0.35 to −0.6 V and also to be independent of the concentration of bismuth in the electrolyte (2.25 and 3 mM). In all cases pulsed electrodeposition resulted in very Te-rich materials by EDX with a trigonal tellurium phase by XRD. In contrast, when applying potentiostatic electrodeposition deposits with much higher bismuth content by EDX were obtained although XRD still showed a trigonal tellurium crystal structure. With similar electrodeposition conditions, there is no significant difference in the compositions of the deposits on bare Pt and on mesoporous silica film-coated Pt substrates. Therefore, the effect of confinement within the mesoporous structure did not affect the composition of the deposit significantly in this study.

Takahashi et al. reported that electrodeposited Bi$_2$Te$_3$ films were composed of two layers with a Te enriched layer nearest the substrate surface [19]. Later, Frantz et al. templated electrodeposited bismuth telluride nanowires from a water/DMSO electrolyte within poly-carbonate etched ion-track membranes covering by a Pt substrate [22]. Similarly, they found the base of the nanowire was tellurium-rich and the cap of the nanowire was bismuth-rich. This variation of composition spreads over the first 500 nm. These observations indicate that at the start stage of electrodeposition, tellurium-rich deposits tend to be obtained. This is consistent with the observation in this study that the short-time pulsed electrodeposition contributes to tellurium-enriched deposits on both bare Pt substrates and mesoporous silica films coated on Pt substrates. In this study, the thickness of film is relatively thin, 100 nm to 200 nm, which is in the very tellurium-rich area in these previous studies.

4. Conclusions

Bismuth, tellurium and bismuth-doped tellurium nanoparticles have been fabricated by templated electrodeposition based on halometallate salts in a non-aqueous system. Silane-grafted mesoporous silica films with three-dimensional orthorhombic mesostructure were used as the templates for electrodeposition. The mesopore size is around 8 nm and the thickness of film is between 100 and 200 nm. A two-step pulsed electrodeposition process was used to deposit into the mesochannels. A variety of deposition conditions was applied to conduct Bi and Te electrodeposition. XRD and EDX shows the presence of Bi and Te. Top-
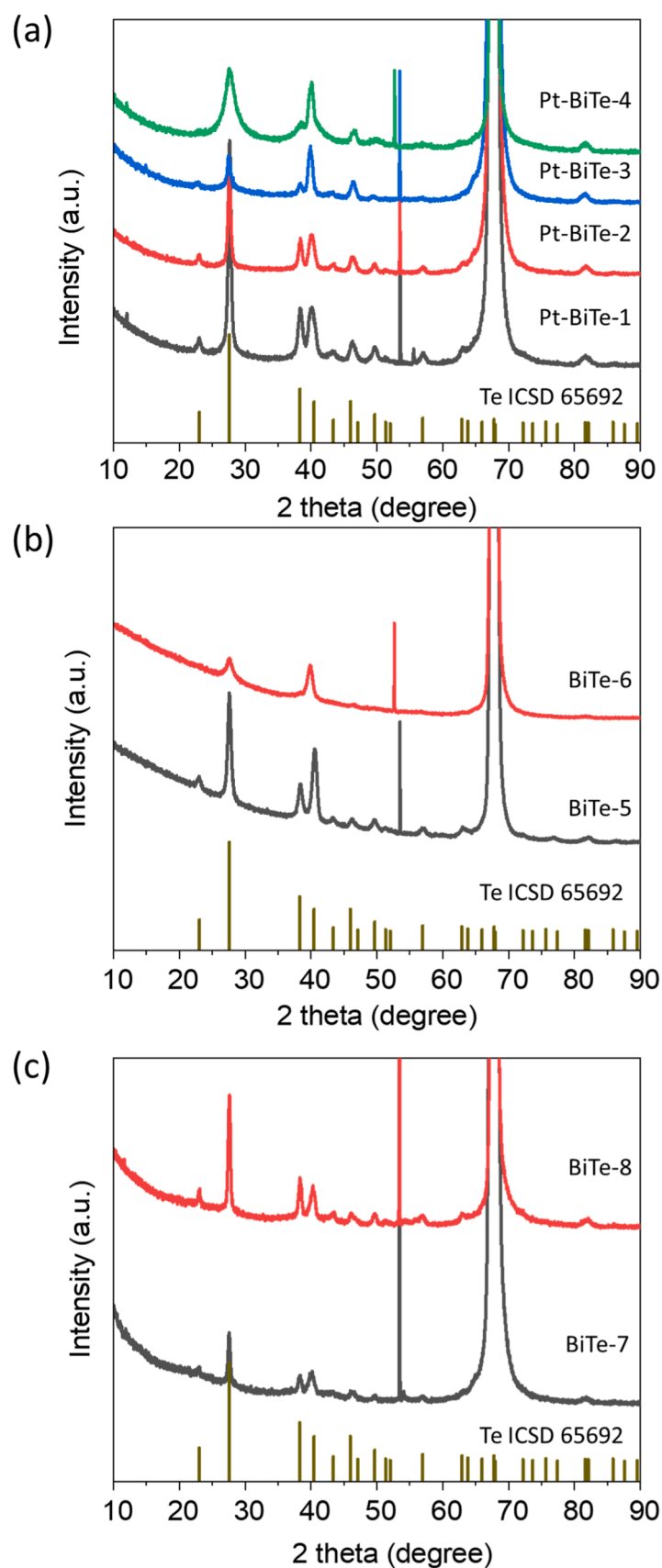
Fig. 8. XRD patterns of Bi-Te deposited on bare Pt substrates (a) and on mesoporous silica film coated-Pt substrates (b,c), the applied electrodeposition conditions were listed in Table 2.

view FE-SEM shows Bi/Te in the mesopores and Bi/Te aggregations on the surface of silica films. Cross-sectional FE-SEM showed a few Te nanowires protruding from individual pores. This showed the possibility to use templated electrodeposition to prepare sub-10 nm nanowires.

A wide range of pulsed electrodeposition conditions were applied for bismuth-tellurium electrodeposition. Top-view FE-SEM showed patchy growth but that some pores were filled by Bi-Te. The deposits are all tellurium-rich, they show trigonal tellurium structure from XRD and very rich tellurium content from EDX. By conducting the same experiments on Pt substrates, it has been demonstrated that confinement within the mesoporous channels does not affect the composition and structure of the electrodeposited Bi-Te in pulsed electrodeposition. Constant electrodeposition time is the essential parameter to influence the composition of the deposit. All samples from pulsed electrodeposition (0.3 s - 5 s) show very low bismuth ratio by EDX (Bi/Te<0.03); the sample of which was electrodeposited for 5 min at -0.6 V achieved high bismuth ratio (Bi/Te=0.49). The deposition current of Te electrodeposition is low in Fig. 2(d) and Figure S1(e,f), while when mixing Bi and Te in the electrolyte, the current increases significantly even though the deposits are mostly tellurium.

CRediT authorship contribution statement

Li Shao: Writing – review & editing, Writing – original draft, Software, Methodology, Investigation, Formal analysis, Conceptualization. **Nikolay Zhelev:** Data curation. **Wenjian Zhang:** Investigation. **Gillian Reid:** Project administration, Conceptualization. **Ruomeng Huang:** Resources. **Philip N. Bartlett:** Project administration, Methodology. **Andrew L. Hector:** Writing – review & editing, Supervision, Methodology, Conceptualization.

Declaration of competing interest

The authors declare that they have no known competing financial interests or personal relationships that could have appeared to influence the work reported in this paper.

Data availability

The original data of electrochemical tests and X-ray diffractions are available on request from the corresponding author Dr Li Shao. The standard X-ray patterns Bi ICSD-64703, Te ICSD-65692 and Bi$_2$Te$_3$ ICSD-7743 can be obtained from Inorganic Crystal Structure Database (ICSD), https://psds.ac.uk/icsd.

Supplementary materials

Supplementary material associated with this article can be found, in the online version, at doi:10.1016/j.electacta.2024.144989.

References

[1] J. Heremans, C.M. Thrush, Y.-M. Lin, S. Cronin, Z. Zhang, M.S. Dresselhaus, J. F. Mansfield, Bismuth nanowire arrays: synthesis and galvanomagnetic properties, Phys. Rev. B 61 (4) (2000) 2921–2930.

[2] Z. Zhang, X. Sun, M.S. Dresselhaus, J.Y. Ying, J. Heremans, Electronic transport properties of single-crystal bismuth nanowire arrays, Phys. Rev. B 61 (7) (2000) 4850–4861.

[3] W. Shim, J. Ham, K.-i. Lee, W.Y. Jeung, M. Johnson, W. Lee, On-film formation of Bi nanowires with extraordinary electron mobility, Nano Lett. 9 (1) (2009) 18–22.

[4] Z. Shi, R. Cao, K. Khan, A.K. Tareen, X. Liu, W. Liang, Y. Zhang, C. Ma, Z. Guo, X. Luo, H. Zhang, Two-dimensional tellurium: progress, challenges, and prospects, Nano-Micro Lett. 12 (1) (2020) 99.

[5] H. Peng, N. Kioussis, G.J. Snyder, Elemental tellurium as a chiral p-type thermoelectric material, Phys. Rev. B 89 (19) (2014) 195206.

[6] K.M. Panahi, K.M. Mousavi, N.M. Salavati, Facile hydrothermal synthesis of tellurium nanostructures for solar cells, J. Nanostruct. 4 (2014) 459–465.

[7] J.-W. Liu, J.-H. Zhu, C.-L. Zhang, H.-W. Liang, S.-H. Yu, Mesostructured assemblies of ultrathin superlong tellurium nanowires and their photoconductivity, J. Am. Chem. Soc. 132 (26) (2010) 8945–8952.

[8] D. Tsiulyanu, S. Marian, V. Miron, H.D. Liess, High sensitive tellurium based NO2 gas sensor, Sens. Actuators B Chem. 73 (1) (2001) 35–39.

[9] D.A. Bograchev, V.M. Volgin, A.D. Davydov, Simulation of inhomogeneous pores filling in template electrodeposition of ordered metal nanowire arrays, Electrochim. Acta 112 (2013) 279–286.

[10] H. Mamur, M.R.A. Bhuiyan, F. Korkmaz, M. Nil, A review on bismuth telluride (Bi2Te3) nanostructure for thermoelectric applications, Renew. Sustain. Energy Rev. 82 (2018) 4159–4169.

[11] Y.L. Chen, J.G. Analytis, J.-H. Chu, Z.K. Liu, S.-K. Mo, X.L. Qi, H.J. Zhang, D.H. Lu, X. Dai, Z. Fang, S.C. Zhang, I.R. Fisher, Z. Hussain, Z.-X. Shen, Experimental realization of a three-dimensional topological insulator, Bi$_2$Te$_3$, Science 325 (5937) (2009) 178–181.

[12] J. Fu, S. Song, X. Zhang, F. Cao, L. Zhou, X. Li, H. Zhang, Bi 2 Te 3 nanoplates and nanoflowers: synthesized by hydrothermal process and their enhanced thermoelectric properties, CrystEngComm 14 (6) (2012) 2159–2165.

[13] I.G. Gonzalez-Martinez, A. Bachmatiuk, V. Bezugly, J. Kunstmann, T. Gemming, Z. Liu, G. Cuniberti, M.H. Rümmeli, Electron-beam induced synthesis of nanostructures: a review, Nanoscale 8 (22) (2016) 11340–11362.

[14] B. Zhou, Y. Zhao, L. Pu, J.-J. Zhu, Microwave-assisted synthesis of nanocrystalline Bi2Te3, Mater. Chem. Phys. 96 (2–3) (2006) 192–196.

[15] J.-W. Liu, F. Chen, M. Zhang, H. Qi, C.-L. Zhang, S.-H. Yu, Rapid microwave-assisted synthesis of uniform ultralong Te nanowires, optical property, and chemical stability, Langmuir 26 (13) (2010) 11372–11377.

[16] H. Zhao, X. Sun, Z. Zhu, W. Zhong, D. Song, W. Lu, L. Tao, Physical vapor deposited 2D bismuth for CMOS technology, J. Semicond. 41 (8) (2020) 081001.

[17] V. Miranda La Hera, X. Wu, J. Mena, H.R. Barzegar, A. Ashok, S. Koroidov, T. Wågberg, E. Gracia-Espino, Controlled synthesis of tellurium nanowires, Nanomaterials 12 (23) (2022) 4137.

[18] T. Sun, X.B. Zhao, T.J. Zhu, J.P. Tu, Aqueous chemical reduction synthesis of Bi2Te3 nanowires with surfactant assistance, Mater. Lett. 60 (20) (2006) 2534–2537.

[19] M. Takahashi, M. Kojima, S. Sato, N. Ohnisi, A. Nishiwaki, K. Wakita, T. Miyuki, S. Ikeda, Y. Muramatsu, Electric and thermoelectric properties of electrodeposited bismuth telluride (Bi2Te3) films, J. Appl. Phys. 96 (10) (2004) 5582–5587.

[20] J. Lee, S. Farhangfar, J. Lee, L. Cagnon, R. Scholz, U. Gösele, K. Nielsch, Tuning the crystallinity of thermoelectric Bi2Te3 nanowire arrays grown by pulsed electrodeposition, Nanotechnology 19 (36) (2008) 365701.

[21] A.W. Zhao, C.H. Ye, G.W. Meng, L.D. Zhang, P.M. Ajayan, Tellurium nanowire arrays synthesized by electrochemical and electrophoretic deposition, J. Mater. Res. 18 (10) (2011) 2318–2322.

[22] C. Frantz, N. Stein, Y. Zhang, E. Bouzy, O. Picht, M.E. Toimil-Molares, C. Boulanger, Electrodeposition of bismuth telluride nanowires with controlled composition in polycarbonate membranes, Electrochim. Acta 69 (2012) 30–37.

[23] P.N. Bartlett, D. Cook, C.H. de Groot, A.L. Hector, R. Huang, A. Jolleys, G. P. Kissling, W. Levason, S.J. Pearce, G. Reid, Non-aqueous electrodeposition of p-block metals and metalloids from halometallate salts, RSC Adv. 3 (36) (2013) 15645–15654.

[24] K. Cicvarić, L. Meng, D.W. Newbrook, R. Huang, S. Ye, W. Zhang, A.L. Hector, G. Reid, P.N. Bartlett, C.H.K. de Groot, Thermoelectric properties of bismuth telluride thin films electrodeposited from a nonaqueous solution, ACS Omega 5 (24) (2020) 14679–14688.

[25] G. Cao, D. Liu, Template-based synthesis of nanorod, nanowire, and nanotube arrays, Adv. Colloid Interface Sci. 136 (1) (2008) 45–64.

[26] C.G. Jin, G.W. Jiang, W.F. Liu, W.L. Cai, L.Z. Yao, Z. Yao, X.G. Li, Fabrication of large-area single crystal bismuth nanowire arrays, J. Mater. Chem. 13 (7) (2003) 1743–1746.

[27] P.N. Bartlett, D.A. Cook, M.M. Hasan, A.L. Hector, S. Marks, J. Naik, G. Reid, J. Sloan, D.C. Smith, J. Spencer, Z. Webber, Supercritical fluid electrodeposition, structural and electrical characterisation of tellurium nanowires, RSC Adv. 7 (65) (2017) 40720–40726.

[28] J. Martín, C.V. Manzano, O. Caballero-Calero, M. Martín-González, High-aspect-ratio and highly ordered 15-nm porous alumina templates, ACS Appl. Mater. Interfaces 5 (1) (2013) 72–79.

[29] T. Nasir, L. Shao, Y. Han, R. Beanland, P.N. Bartlett, A.L. Hector, Mesoporous silica films as hard templates for electrodeposition of nanostructured gold, Nanoscale Adv. 4 (22) (2022) 4798–4808.

[30] R.D. Reeves, L.A. Crosser, G.E. Chester, J.J. Hill, Thermoelectric property enhancement via pore confinement in template grown bismuth telluride nanowire arrays, Nanotechnology 28 (50) (2017) 505401.

[31] J. Heremans, C.M. Thrush, Thermoelectric power of bismuth nanowires, Phys. Rev. B 59 (19) (1999) 12579–12583.

[32] S. Li, H. Zhang, H. Ruan, Z. Cheng, Y. Yao, F. Zhuge, T. Zhai, Programmable nucleation and growth of ultrathin tellurium nanowires via a pulsed physical vapor deposition design, Adv. Funct. Mater. 33 (11) (2023) 2211527.

[33] D. Zhao, P. Yang, N. Melosh, J. Feng, B.F. Chmelka, G.D. Stucky, Continuous mesoporous silica films with highly ordered large pore structures, Adv. Mater. 10 (16) (1998) 1380–1385.

[34] X. Huang, H. Mutlu, P. Théato, The toolbox of porous anodic aluminum oxide–based nanocomposites: from preparation to application, Colloid Polym. Sci. 299 (3) (2021) 325–341.

[35] Paar, A. Pore Size Measurement of Track Etched Membranes by Capillary Flow Porosimetry. https://www.anton-paar.com/corp-en/services-support/documen t-finder/application-reports/pore-size-measurement-of-track-etched-membranes -by-capillary-flow-porosimetry/.

[36] A. Fukuoka, H. Araki, Y. Sakamoto, N. Sugimoto, H. Tsukada, Y. Kumai, Y. Akimoto, M. Ichikawa, Template synthesis of nanoparticle arrays of gold and platinum in mesoporous silica films, Nano Lett. 2 (7) (2002) 793–795.

[37] L. Meng, K. Cicvarić, A.L. Hector, C. de Groot, P.N. Bartlett, Electrodeposition of bismuth telluride from a weakly coordinating, non-aqueous solution, J. Electroanal. Chem. 839 (2019) 134–140.

[38] Y.J. Noori, L. Meng, A.H. Jaafar, W. Zhang, G.P. Kissling, Y. Han, N. Abdelazim, M. Alibouri, K. LeBlanc, N. Zhelev, Phase-change memory by GeSbTe electrodeposition in crossbar arrays, ACS Appl. Electron. Mater. 3 (8) (2021) 3610–3618.

[39] G.E.B.Y. Ahlijah, M. Goldstein, Vibrational spectra of tetrahalogeno-complexes of antimony(III) and bismuth(III), Chem. Commun. (London) (21) (1968) 1356–1358.

[40] P.J. Hendra, Z. Jović, The Raman spectra of some complex anions of formula [MX6]2– in the solid phase and in solution, where M = Se and Te; X = Cl, Br, and I, J. Chem. Soc. A Inorg. Phys. Theor. (0) (1968) 600–602.

[41] G.Y. Ahlijah, M. Goldstein, Far-infrared and Raman spectra of tetrahalogeno-complexes of arsenic(III), antimony(III), and bismuth(III), J. Chem. Soc. A Inorg. Phys. Theor. (0) (1970) 326–329.

[42] D.A. Couch, C.J. Wilkins, G.R. Rossman, H.B. Gray, Electronic energy levels in hexahalotellurate(IV) complexes, J. Am. Chem. Soc. 92 (2) (1970) 307–310.

[43] D.A. Cook, S.J. Reeves, W. Zhang, G. Reid, W. Levason, P.N. Bartlett, J.M. Dyke, V. K. Greenacre, Tellurium electrodeposition from tellurium(II) and (IV) chloride salts in dichloromethane, Electrochim. Acta 456 (2023) 142456.

[44] L. Meng, K. Cicvarić, A.L. Hector, C.H. de Groot, P.N. Bartlett, Electrodeposition of bismuth telluride from a weakly coordinating, non-aqueous solution, J. Electroanal. Chem. 839 (2019) 134–140.

[45] Z. He, Y. Yang, J.-W. Liu, S.-H. Yu, Emerging tellurium nanostructures: controllable synthesis and their applications, Chem. Soc. Rev. 46 (10) (2017) 2732–2753.

[46] P. Cucka, C.S. Barrett, The crystal structure of Bi and of solid solutions of Pb, Sn, Sb and Te in Bi, Acta Crystallogr. 15 (9) (1962) 865–872.

[47] C. Adenis, V. Langer, O. Lindqvist, Reinvestigation of the structure of tellurium, Acta Crystallogr. Sect. C 45 (6) (1989) 941–942.

[48] V.R. Akshay, M.V. Suneesh, M. Vasundhara, Tailoring thermoelectric properties through structure and morphology in chemically synthesized n-type bismuth telluride nanostructures, Inorg. Chem. 56 (11) (2017) 6264–6274.

[49] C. Jin, X. Xiang, C. Jia, W. Liu, W. Cai, L. Yao, X. Li, Electrochemical fabrication of large-area, ordered Bi2Te3 nanowire arrays, J. Phys. Chem. B 108 (6) (2004) 1844–1847.